The effect of Equal Channel Angular Pressing on the stress corrosion cracking susceptibility of AZ31 alloy in simulated body fluid

Mirco Peron [a,*], Pål Christian Skaret [b], Alberto Fabrizi [c], Alessandra Varone [d], Roberto Montanari [d], Hans Jørgen Roven [b], Paolo Ferro [c], Filippo Berto [a], Jan Torgersen [a]

[a] Department of Industrial and Mechanical Engineering, Norwegian University of Science and Technology, Richard Birkelands vei, 2b, 7034, Trondheim, Norway
[b] Department of Materials Science and Engineering, Norwegian University of Science and Technology, Alfred Getz vei, 2, 7491, Trondheim, Norway
[c] Department of Management and Engineering, Padova University, Stradella San Nicola, 3, 36100, Vicenza, Italy
[d] Department of Industrial Engineering, University of Rome "Tor Vergata", Via del Politecnico, 1, 00133, Rome, Italy

A B S T R A C T

Despite the great potential of Mg and its alloys as material for biodegradable implants, their low resistance to the simultaneous action of corrosion and mechanical stresses in the human body have hampered their use. Stress Corrosion Cracking has been reported as one of the most critical failure modes to overcome to allow such materials to be clinically applied. Thus, in this paper we investigate the effect of Equal Channel Angular Pressing (ECAP) on the Stress Corrosion Cracking (SCC) susceptibility of the AZ31 Mg alloy. To do so, AZ31 alloy has been subjected to 1, 2 and 4 passes of ECAP, and the samples so obtained have then been tested by means Slow Strain Rate Tests (SSRTs) in Simulated Body Fluid (SBF) at 37 °C. Samples subjected to one pass of ECAP are shown to be less susceptible to SCC compared to the material in the as-received condition, while further ECAP processing (2 and 4 passes) are found to worsen the SCC susceptibility. To understand the different SCC susceptibilities shown by the differently ECAPed samples, microstructural analyses, potentiodynamic polarization curves, hydrogen evolution experiments and Scanning Electron Microscopy (SEM) analyses of the fracture surfaces were carried out. The improved corrosion resistance of the samples subjected to 1 pass of ECAP compared to the samples in the as received condition (due to a finer grain size) and to the samples subjected to 2 and 4 passes (due to a more favourable texture evolution) represents the reason of their reduced SCC susceptibility.

1. Introduction

In the past years, the amount of people undergoing surgical procedures involving the implantation of medical devices is continuously growing (Ginebra et al., 2006). In particular, orthopaedic surgery is the most important, with the associated healthcare system costs estimated to increase by 26% in 2030 compared to 2019 in Europe (share.iofbone-health). The materials currently used in orthopaedic surgery are permanent metallic materials, such as stainless steel, titanium, and cobalt-chromium alloys (Chen and Thouas, 2015). In particular, these inert materials are used as load-bearing implants for replacement of diseased or damaged tissues (Hanawa, 2010; Albrektsson et al., 1981; Rossi et al., 2014). However, two main disadvantages are linked to the implementation of these materials. Firstly, the great difference in elastic modulus of these materials compared to that of human bone results in the occurrence of the stress-shielding phenomenon. This is a consequence of stress distribution changes between the bone and the implant (Bauer and Schils, 1999; Dujovne et al., 1993; Engh and Bobyn, 1988; Kerner et al., 1999; Sumner and Galante, 1992; Turner et al., 1997; Van Rietbergen et al., 1993): bones adapt to the reduced stress field according to the Wolff's law (Wolff, 1986), resulting in the bone either becoming more porous (internal remodelling) or thinner (external remodelling), leading to a higher risk of implant failure. Secondly, after the bone has healed, permanent metals must be removed from the body by using a secondary surgical intervention since they can lead to long-term complications, such as local inflammations due to the potential release of cytotoxic ions as a consequence of corrosion or wear processes (Pound, 2014a, 2014b; Jacobs et al., 1998, 2003; Beech et al., 2006). To solve these drawbacks, biodegradable materials like magnesium and iron alloys have been proposed in medical science as a novel class of highly bioactive materials. That is, these materials are supposed to temporarily aid the healing process of a diseased tissue or organ and

then they can progressively disappear by virtue of body fluids corrosion after a certain length of functional use, leading to simultaneous implant replacement through the surrounding tissue (Peron et al., 2017). Magnesium is one of the most promising candidates for biodegradable applications due to its excellent bio-compatibilities with human physiology and the best mechanical compatibility with human bone (Singh Raman et al., 2015). Its low density and elastic modulus best mimic the properties of natural bones, reducing the risk of the stress shielding phenomenon (Peron et al., 2017). Moreover, Mg is the fourth most abundant element in the human body (it is recommended that an adult receives 240–420 mg daily and any excess can be harmlessly excreted in the urine (Staiger et al., 2006)). Finally, it is essential for the metabolism in many biological mechanisms, being a cofactor for many enzymes (Hänzi et al., 2009), and Mg^{2+} ions resulting from the degradation process are reported to aid the healing and growth of tissue. However, the greatest limitation of Mg consists of its fast corrosion rate, especially in human body fluid containing chloride, giving rise to immature drop in mechanical integrity of the device before accomplishing its defined mission (Song, 2007). Over and above corrosion rate, critical hydrogen gas bubbles and alkalization resulting from corrosion of Mg in body fluid are also other problematic subjects in fast corrosion-rate processes, leading to accumulation of evolved hydrogen bubbles in gas pockets next to the implant and consequently, causing necrosis of tissues. However, if the corrosion rate of Mg implant can be suitably controlled, hydrogen evolution will not be rapid enough to cause critical subcutaneous bubbles, and the alkalization effect could be easily balanced by metabolic mechanisms in the human body. A further challenging issue to be faced concerns the fact that the implant must possess adequate resistance to cracking under the simultaneous action of the corrosive human body fluid and the mechanical loading characteristics of the human body. Corrosion-assisted cracking phenomena, such as stress corrosion cracking (SCC) and corrosion fatigue (CF), were in fact reported to cause the failure of several traditional implants (Teoh, 2000; Akahori et al., 2000; Jafari et al., 2015; Antunes and de Oliveira, 2012). In particular, SCC is particularly dangerous because it leads to a sudden and catastrophic fast failure under mechanical loading conditions otherwise considered to be safe, and magnesium and its alloys have been reported to be susceptible to it in simulated physiological conditions (Jafari et al., 2017, 2018; Kannan and Raman, 2008). Therefore, it is important to develop Mg-based implants that confer a combination of strength and corrosion resistance in human body fluid without causing corrosion-assisted cracking phenomena. However, most studies have focused on improving the electrochemical properties of Mg and its alloys, whereas the literature on improving their resistance to corrosion-assisted cracking phenomena is very limited. In fact, while different procedures have been applied in the recent years to improve their corrosion resistance, from alloying to surface modification techniques, only few of them have been assessed regarding their effects on the susceptibility to corrosion-assisted cracking phenomena. Mohajernia et al. (2018) reported that hydroxyapatite coating containing multi-walled carbon nanotubes reduced the corrosion current density of AZ31 alloy of three order of magnitude. In addition, they reported the elongation to failure of AZ31 samples subjected to slow strain rate tests (SSRT) in simulated body fluid (SBF) at 37 °C to be increased about 70% with the application of the coating. These results agree with those obtained by Chen et al. (2018). They coated Mg-4Zn-0.6Zr-0.4Sr with a composite coating consisting of a poly (lactic-co-glycolic acid) (PLGA) superimposed to a micro-arc oxidation (MAO) layer and they reported this composite coating to increase the elongation to failure of the bare alloy subjected to SSRT in modified simulated body fluid (m-SBF) at 37 °C from 5% to 11%. Again, the corrosion rate was reduced of three order of magnitude. However, when repetitive loadings are applied, the presence of coatings might result to be detrimental for the fatigue life of the implants due to the formation of cracks in the coating (due to elastic modulus mismatch) that act as stress concentrators and also due to the generally higher surface roughness of the coated samples compared to

the polished uncoated counterparts (Gao et al., 2015). Alternatively, alloying has been reported as a valuable solution to improve the corrosion resistance of Mg and the effect of different alloying elements on the corrosion-assisted cracking phenomena. For instance, Kannan et al. (Bobby Kannan et al., 2008), compared the SCC susceptibility of three different rare earth (RE)-containing alloys, namely ZE41, QE22 and EV31A, with that of AZ80 alloy. They suggested that rare-earth elements in magnesium alloys can improve the SCC resistance significantly, being EV31A alloy the most resistant to SCC compared to the other alloy. The beneficial effect of RE was found also by Choudhary et al. (2014). According to their findings, a lower SCC susceptibility was observed for RE-containing alloys, i.e. WZ21 and WE43 compared to Mg-Zn-Ca alloy (ZX50). However, some RE elements were reported to be toxic for the human body (Rim et al., 2013), and in general alloying may introduce elements that lead to adverse biological reactions. In recent years, mechanical processing inducing severe plastic deformation (SPD) have been investigated as an alternative to alloying and coating techniques. Again, broad attention was given to the effect of SPD techniques on the corrosion properties, whereas very few on the SCC susceptibility. Machining has been studied as method to reduce the corrosion rate. In particular, cryogenic machining has attracted researcher's attention on its effect on the corrosion behaviour of Mg alloys. Bertolini et al. reported dry machined AZ31 samples to be characterized by an hydrogen evolution rate twice that of the cryogenic machined counterparts (Bertolini et al., 2017). In addition, Peron et al. (2020) reported the elongation to failure of AZ31 samples subjected to slow strain rate tests (SSRT) in simulated body fluid (SBF) at 37 °C to be increased only about 30% with the cryogenic machining. These improvements were associated with the formation of a nano-crystalline and compressed surface layer. However, once the nano-crystalline surface layer dissolves, the machining induced corrosion resistance disappears. Recently, Equal Channel Angular Pressing (ECAP) has been proved to induce a very fine and homogeneous microstructure throughout all the samples. Broad attention was given to the effects of ECAP on the corrosion properties, whereas very few on the SCC susceptibility. Dealing with the corrosion behavior, the effects of ECAP still remain uncertain. In fact, some researchers reported that ultrafine-grained Mg alloy produced by ECAP deteriorated the corrosion resistance (Song et al., 2019; Kutniy et al., 2009; Witecka et al., 2016), whereas other works observed improved performances after ECAP (Wang et al., 2008; Linderov et al., 2017; Minárik et al., 2017). This work aims thus to provide further insight into the effects of ECAP on the corrosion resistance. One, two and four passes of ECAP have thus been applied on AZ31 alloy and the corrosion behaviour has been assessed. To this aim, both potentiodynamic polarization curves and hydrogen evolution tests were used. The as-received material has also been tested as reference. In addition, for the first time to the best of the authors' knowledge, the effect of ECAP on the SCC susceptibility has been investigated. Slow strain rate tests (SSRT) at a strain rate of $3.5 \cdot 10^{-6}$ s^{-1} have been carried out on one, two and four ECAPed AZ31 samples. The samples were immersed for the whole duration of the tests in SBF at 37 °C. Fracture surfaces were analyzed by means of scanning electron microscopy (SEM) to provide a better understanding of the different failure mechanisms shown by the different ECAP-treated samples.

2. Materials and methods

2.1. Material and ECAP processing

In this study, ECAP was performed on AZ31 magnesium alloy. The commercially available bars (Dynamic Metals Ltd, Bedfordshire, UK) were machined into square billets with 19.7 mm side and 100 mm length. ECAP pressing was conducted through a die with an internal angle (Φ) of 90° between the vertical and the horizontal channels and a curvature angle (ψ) of 20° (Fig. 1).

The ECAP temperature was set as 250 °C to avoid the formation of

extensive cracking that otherwise would have formed due to a lack of adequate ductility (Ge et al., 2013). The die was homogeneously heated by 4 electrical resistance heaters placed along the vertical channel and at the intersection point of the channels. The temperature was monitored throughout the process using a thermocouple inserted in the die in the proximity of the sample. Repetitive pressings of the same sample were performed up to a maximum of 4 passes by rotating in the same direction the sample along their longitudinal axis by 90° before each new pass (route B_c according to established designation given in the literature (Segal, 1999). The billets were pressed into the ECAP die with a speed of 1 mm/min using molybdenum disulphide (MoS_2) as lubricant. The tensile testing machine used for this operation was an MTS 311 (1000kN) (MTS, MN, USA).

2.2. Microstructural observation

Microstructural characterizations were performed on the as-received alloy and the ECAP processed billets. Samples were cut along their longitudinal cross-section, polished up to mirror finishing surface with silica colloidal suspension and, finally, etched using a solution of 10 ml H_2O, 10 ml acetic acid, 80 ml ethanol and 4.2 g picric acid. The microstructure was analyzed using a Leica DMRETM Optical Microscope (Leica microsystems, Wetzlar, Germany).

2.3. Mechanical characterization

The mechanical properties were characterized by means of uniaxial tensile tests and Vickers hardness measurements. The tensile tests were conducted on dogbone cylindrical samples having the gauge length of 20 mm and the diameter of 4 mm. The specimens were machined from the billets parallel to the ECAP direction. Each specimen was pulled to failure using an Instron 5969 testing machine (MA, USA) with a 50 kN load cell to obtain the load–displacement curves of the fabricated samples. A strain rate of $3.5 \cd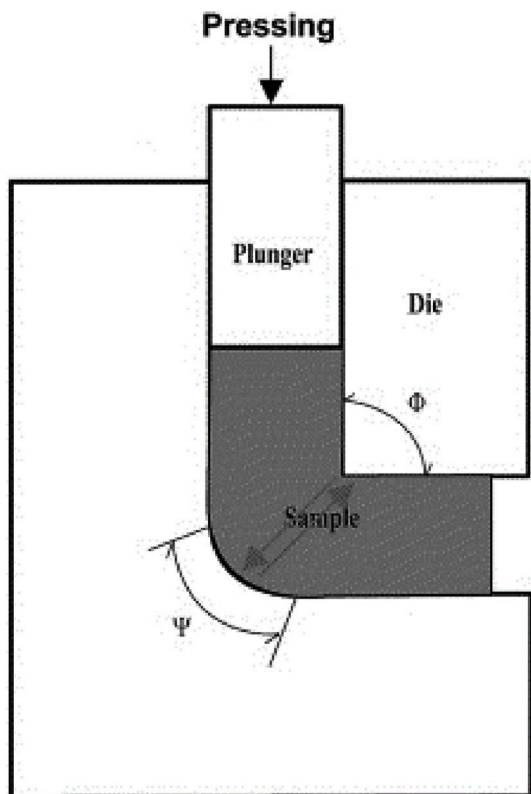ot 10^{-6}\, s^{-1}$ was used to conduct tensile tests under strain control mode. The reported results are averaged over three tests. The Vickers hardness tests were conducted on the plane perpendicular to the ECAP direction in accordance with ASTM E92 standard (ASTM E92, 2017). The surfaces of the sections were ground and mechanically polished to a mirror-like finish with silica colloidal suspension. The hardness tests were carried out at ambient temperature using a load of 100 g and a holding time of 15 s. The values of Vickers hardness (HV) were recorded using a Struers Duramin-A300 hardness tester equipped with a Vickers diamond indenter. An average over at least seven separate measurements taken at randomly selected points was used to measure the mean values of HV.

2.4. Corrosion performance evaluation

The corrosion performances of the as-received and of the ECAPed AZ31 alloy were measured by means of potentiodynamic polarization curves and hydrogen evolution experiments. In order to perform the former, small parallelepipeds with a thickness of 2 mm and a square face of 16 mm side were manufactured from the as-received bars and from the billets subjected to one, two and four passes of ECAP. The samples obtained this way were first polished with 2000 and then with 4000 grit silicon carbide papers and then cleaned with acetone and ethanol for five minutes in ultrasonic bath prior to testing. To perform the hydrogen evolution tests, the as-received bars and the billets subjected to one, two and four passes of ECAP were machined into small cubes with a 10 mm side, respectively. Again, prior to testing, the cubes were first polished with 2000 and then with 4000 grit silicon carbide papers and then cleaned with acetone and ethanol for five minutes in ultrasonic bath.

2.4.1. Potentiodynamic polarization curves

Potentiodynamic polarization tests were carried out on a Gamry Interface 1000 potentiostat (Gamry Instruments, PA, USA) in order to compare the effects of the ECAP process on the corrosion resistance. Samples obtained from the as-received material and from the billets subjected to one, two and four passes of ECAP were tested. The electrochemical tests used three-electrode equipment with the as-received or the ECAPed samples as a working electrode, a Hg/Hg_2SO_4 electrode as a reference electrode, and a platinum plate electrode as a counter electrode. The samples were immersed in SBF solution (composition reported in Table 1). The temperature was set to $37 \pm 1\ °C$ to reproduce human body conditions. The potentiodynamic polarization curves were obtained applying a potential from ± 2 V with respect to the open circuit potential (OCP), obtained after a stabilization period of 30 min. The scan rate of the potentiodynamic polarization test was 0.5 mV/s. The area of the samples exposed to SBF was 1 cm^2 and corrosion current density were determined using the Tafel extrapolation method, according to the ASTM G5-14 standard (ASTM G5 - 14). The tests were repeated three times for each condition.

2.4.2. Hydrogen evolution tests

The corrosion of one mole Mg leads to the evolution of one mole of

Fig. 1. Schematic illustration of die configuration for ECAP processing.

Table 1
Reagents and their quantities for preparation of 1000 ml of the SBF solution according to Kokubo and Takadama (2006).

Reagents	Amount
NaCl	8.035 g
NaHCO$_3$	0.355 g
KCl	0.225 g
K$_2$HPO$_4$·3H$_2$O	0.231 g
MgCl$_2$·6H$_2$O	0.311 g
1.0$_M$-HCl	39 ml
CaCl$_2$	0.292 g
Na$_2$SO$_4$	0.072 g
Tris	6.118 g

hydrogen gas. This allows the measurement of Mg's corrosion rate through the collection of evolving hydrogen gas bubbles. Hence, hydrogen evolution tests were used to assess the effects of the ECAP process for improving corrosion resistance. The samples described in Section 2.4. were obtained from the as-received material and from the billets subjected to one, two and four passes of ECAP and were immersed individually in SBF at 37 °C for 96 h. From each sample, the hydrogen bubbles were collected in a burette (Fig. 2), according to an established protocol published elsewhere (Song et al., 2013).

2.5. Stress corrosion cracking (SCC) susceptibility

Slow strain rate tests are a common technique used for studying the combined effect of stress and corrosion/degradation process on the mechanical properties of a material, and they have been used in this work to investigate the effect of ECAP on the SCC susceptibility. The SSRT experiments were carried out on the as-received and ECAPed dog-bone samples described in Section 2.3. at a strain rate of $3.5 \cdot 10^{-6}$ s^{-1} in SBF solution at body temperature (37 ± 1 °C). The strain rate value was chosen according to Bobby Kannan et al. (2008) to render the AZ31 alloy susceptible to SCC. A schematic representation of the experimental set-up is shown in Fig. 3. The sample was immersed for the whole duration of the test and the SBF solution was constantly changed by a pumping system. The SBF solution container was immersed in a water bath, which's temperature was constantly monitored with a thermometer. When the temperature was below its set value, a commercial resistance heating element placed inside the water bath automatically turned on until the desired temperature was reached again. In addition, while carrying out the SSRTs, the area of the specimen exposed to SBF was restricted to its gauge length using Teflon tapes wrapping the rest of the specimen, thus maintaining a constant area of exposure to the corrosive solution as well as avoiding the possibility of galvanic effects with other components of the testing set-up. For sake of comparability, the
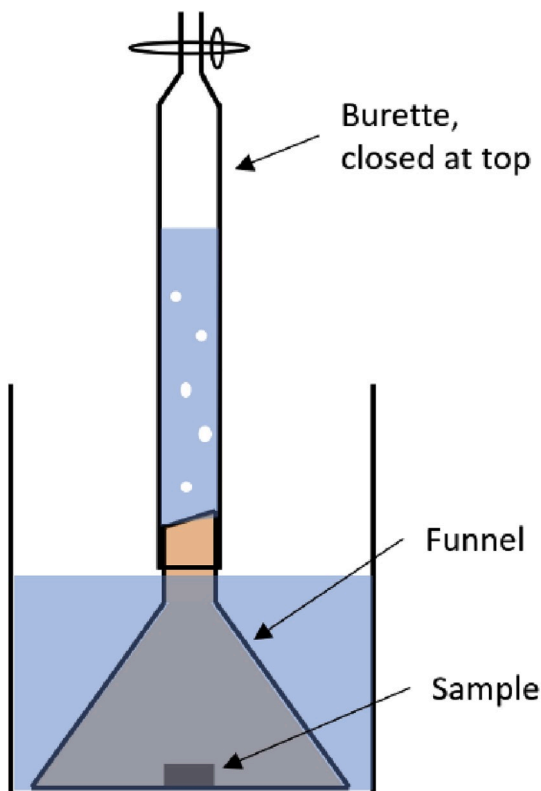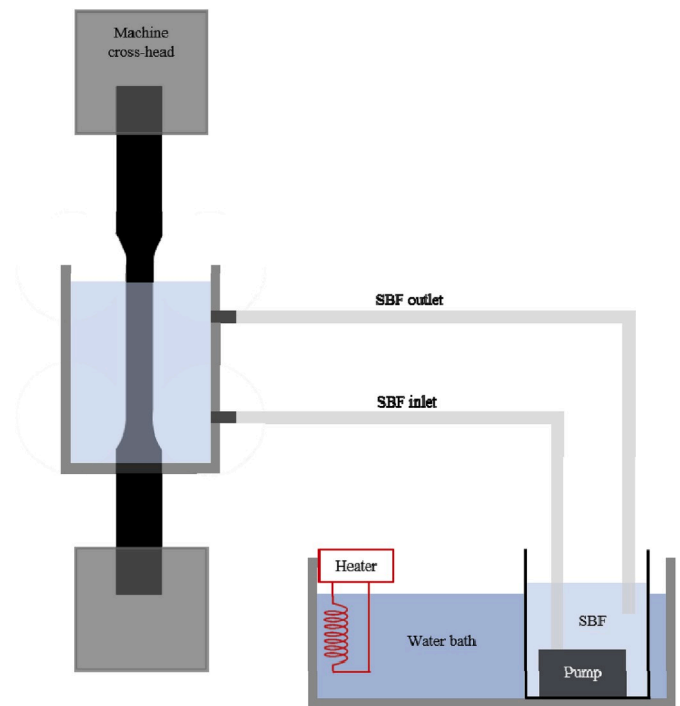

Fig. 3. Schematic representation of the SSRT set-up.

results obtained from the mechanical characterizations (Section 2.3.) were used as reference in air.

The gauge length of the specimens were polished up to 4000 grit silicon carbide papers and then cleaned with ethanol prior to testing as suggested in other works (Jafari et al., 2017, 2018; Choudhary and Raman, 2011). SSRTs were repeated three times for reproducibility.

In order to quantify the AZ31 SCC sensitivity, the susceptibility indices I_{UTS} and I_{ε} were calculated according to Eq. (1) and Eq. (2) (Choudhary et al., 2014):

$$I_{UTS} = \frac{UTS_{air} - UTS_{SBF}}{UTS_{air}} \tag{1}$$

and

$$I_{\varepsilon} = \frac{\varepsilon_{air} - \varepsilon_{SBF}}{\varepsilon_{air}} \tag{2}$$

where UTS is the Ultimate Tensile Strength and ε the elongation at failure, both evaluated during tests conducted in SBF solution and air. When the value of the susceptibility index approaches zero, the material is considered to be highly resistant to SCC, namely the greater the index the greater the susceptibility to SCC.

2.6. Fractography

The specimen fracture surfaces of the samples tested in air and in SBF were observed by means of a FEI Quanta 450 Scanning Electron Microscope (Thermo Fisher Scientific Inc., USA). Prior to fractographic evaluations, the samples tested in the corrosive environment were cleaned from the corrosion products by immersion for one minute in a solution prepared using 50 g chromium trioxide (CrO_3), 2.5 g silver nitrate ($AgNO_3$) and 5 g barium nitrate ($Ba(NO_3)_2$) in 250 ml distilled water, as suggested elsewhere (Thirumalaikumarasamy et al., 2014). Both the samples tested in air and in SBF were washed with distilled water and finally ultrasonically cleaned in acetone for 10 min before the fractographic evaluations.

Fig. 2. Schematic illustration of the set-up for the measurement of the evolved hydrogen volume.

3. Results

3.1. Microstructural observation

Fig. 4 presents optical microstructures of the as-received material (a) and those of the material ECAPed by 1 pass (b), 2 passes (c) and 4 passes (d). Their equivalent diameter distributions determined by means of an image analysis software (Leica Application Software v.3.8, Leica Microsystems, Wetzlar, Germany) are reported in Fig. 5 and in Table 2.

The as-received material exhibits large grains (Fig. 4a) with a broad grain size distribution (Fig. 4a) and an average grain diameter of 27.5 μm; moreover, the microstructure is characterized by almost equiaxed grains. After 1 pass, the material displays a heterogeneous microstructure (Fig. 4b) so-called "bimodal" grain structure (Xia et al., 2005) consisting of coarse grains, that are reported to be the un-recrystallized grains from the initial state (Gzyl et al., 2014), surrounded by colonies of very fine grains, nucleated along the grain and twin boundaries through dynamic recrystallization (DRX) (Figueiredo and Langdon, 2010). For this process condition, the average grain diameter decreases to 8.3 μm. In addition, the broad roundness distribution (Fig. 6b) reveals that the grains are significantly distorted and elongated due to the plastic shear deformation after 1 pass. On the contrary, the microstructure of the material after 2 passes significantly changes and now comprises a uniform grain structure with fine equiaxed grains and an average diameter of 6.8 μm (Fig. 5c). The grain structure after 4 passes is almost equivalent to the material after 2 passes: the average grain size is still 6.5 μm (Fig. 5d) but the grain roundness distribution is narrower and more peaked close to the unit (Fig. 6d). Therefore, even if processing the material by 4 ECAP passes at 250 °C do not induce a further grain refinement of the alloy due to the grain nucleation stimulated by high temperature during strain accumulation (Bryła et al., 2012), it produces a totally recrystallized and equiaxed microstructure.

3.2. Mechanical characterization

In Table 3, the Vickers hardness of the as-received and the 1, 2 and 4 ECAPed passed material is presented.

The Vickers hardness value of AZ31 alloy slightly increases after 1 pass of ECAP, but 2 passes of ECAP leads to its reduction towards a value comparable to the as-received condition. Further ECAPing leads to a further reduction of the Vickers hardness.

The engineering stress-strain curves of the as-received and the 1, 2 and 4 passes ECAPed specimens are presented in Fig. 7. In addition, Table 4 compares the yield strength (σ_y), the UTS and the elongation at failure obtained from the curves in Fig. 7.

The data demonstrated that both the yield and ultimate tensile strength and the elongation to failure increases after 1 pass of ECAP. However, further ECAP passes lead to a continuous decrease in the yield strength whereas to a continuous increase in ductility (the elongation to failure after 4 passes of ECAP is more than 3 times higher than the elongation to failure of the as-received material).

3.3. Corrosion performance evaluation

3.3.1. Potentiodynamic polarization curves

The potentiodynamic polarization curves of the AZ31 cylindrical samples in SBF plotted on a semi-logarithmic scale are shown in Fig. 8. The related kinetic and thermodynamic corrosion electrochemical characteristics are reported in Table 5. The effect of ECAP on the corrosion resistance is of complex nature. One pass of ECAP leads to a reduced corrosion current density, and thus to an improved corrosion resistance since the corrosion current density is directly related to the corrosion rate, whereas further ECAP passes are found to worsen the corrosion resistance. It is worth to note that the corrosion current density of 2 and 4 ECAPed AZ31 alloy is even worse than that of the as-received material.

3.3.2. Hydrogen evolution tests

The results from the hydrogen evolution tests are reported in Fig. 9.

The results from the hydrogen evolution tests agree with those obtained from potentiodynamic polarization curves. 1 pass of ECAP leads to a reduction in the amount of hydrogen evolved compared to the as-
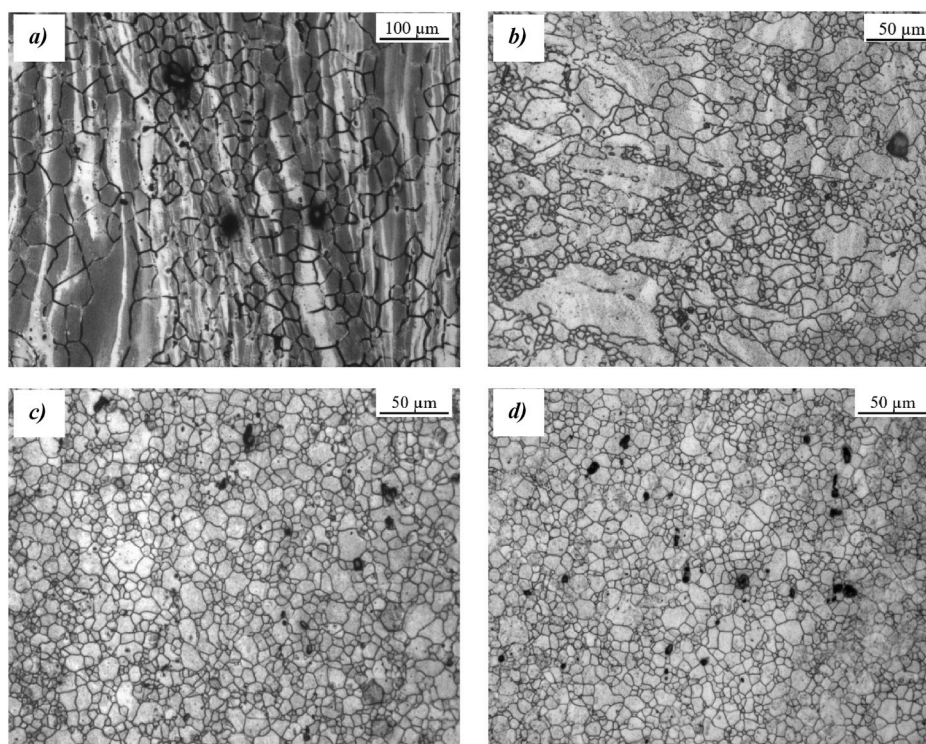

Fig. 4. Micrograph of AZ31 alloy at the (a) as-received condition and after (b) 1 pass, (c) 2 passes and (d) 4 passes of ECAP; note the different scale bar in (a).
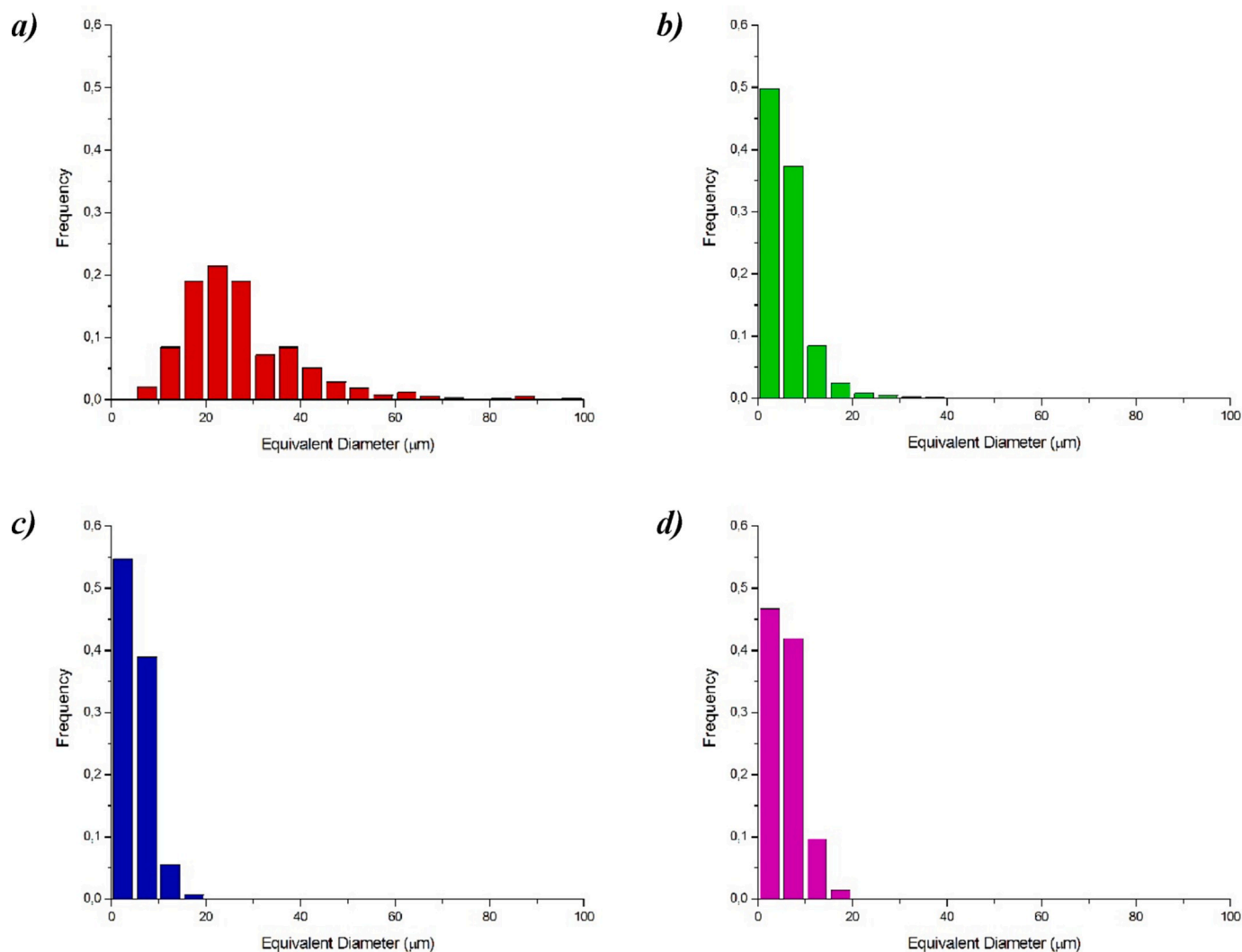
Fig. 5. Equivalent diameter distribution of AZ31 alloy at the (a) as-received condition and after (b) 1 pass, (c) 2 passes and (d) 4 passes of ECAP.

received material. However, 2 passes of ECAP lead to a deterioration in the corrosion resistance since the hydrogen evolved from the AZ31 alloy treated with 2 passes of ECAP is slightly higher than that of the as-received counterpart. Furthermore, further ECAP processing (4 passes) leads to a further increase of the amount of hydrogen evolved.

3.4. Stress corrosion cracking susceptibility

Fig. 10 shows the engineering stress-strain curve of the as-received material (a) and that of the material ECAPed by 1 pass (b), 2 passes (c) and 4 passes (d) tested in SBF. For sake of comparison, the corresponding engineering stress-strain curves of the materials tested in air are reported. Finally, Fig. 10e shows the comparison of the samples tested in SBF.

In addition, Table 6 compares the UTS and the elongation to failure values obtained from the curves in Fig. 10.

From the considerably reduced elongation at failure it can be seen that the alloy suffered embrittlement in SBF regardless the adoption of ECAP treatments. It is however worth noting that the introduction of ECAP processing led to an increased elongation at fracture.

To quantify the SCC susceptibility of the as-received and ECAPed material, the I_{UTS} and I_{ε} indices were evaluated and are reported in Fig. 11.

The SCC indexes reveals that after one pass of ECAP, the SCC susceptibility of the alloy was highly reduced, i.e. by 67% and 47% for I_{UTS}

and the I_{ε}, respectively. However further ECAP treatments led to a worsening of the SCC indexes. In fact, I_{UTS} increased from 4.8% for 1 pass of ECAP to 8.2% and 19.3% for 2 and 4 passes, respectively, while I_{ε} increased from 28.9% to 58.1% and 68.2% for 2 and 4 passes, respectively. This suggests that the lowest SCC susceptibility indexes were obtained for the material treated with 1 pass of ECAP, that also leads to the highest UTS and elongation to failure when tested in SBF.

3.5. Fractography

3.5.1. Samples tested in air

The fracture surfaces of the samples tested in air are reported in Fig. 12, and in particular the fractographies of the samples in the as-received condition are reported in Fig. 12a and e, while those of the ECAPed samples are reported in Fig. 12b and f, Fig. 12c and g and Figs. 12d and h for 1, 2 and 4 passes of ECAP, respectively.

From the SEM pictures it can be seen that in the alloy in the as-received condition a predominant feature of the fracture surfaces is the occurrence of cleavage. This agrees with the reduced ductility shown by the mechanical tests in Fig. 7 (red curve). After one pass of ECAP the fracture morphologies show a mixed fracture mode of ductile-brittle type with the typical combination of dimples and cleavage planes. This change in fracture morphology reveals an enhanced ductility, which is confirmed by the mechanical tests (green curve in Fig. 7). Further ECAP processing leads to the transition from the mixed ductile-
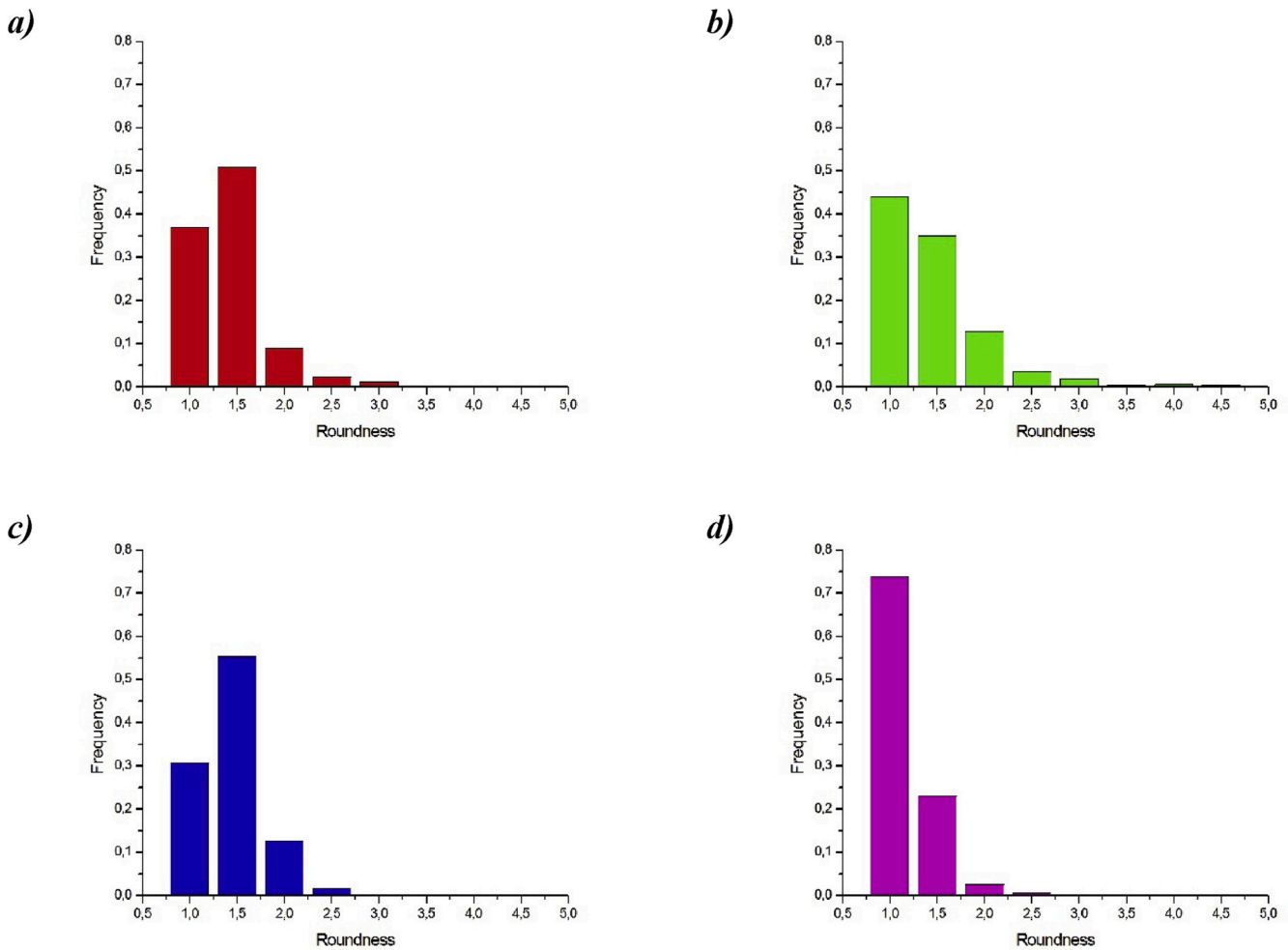
Fig. 6. Grain roundness distribution of AZ31 alloy at the (a) as-received condition and after (b) 1 pass, (c) 2 passes and (d) 4 passes of ECAP.

Table 2
Equivalent diameter and roundness from Figs. 5 and 6.

	As-received	ECAP		
		1 pass	2 passes	4 passes
Equivalent Diameter	27.5 ± 13.4	8.3 ± 5.2	6.8 ± 2.8	6.5 ± 3.1
Roundness	1.7 ± 0.3	1.9 ± 0.6	1.5 ± 0.3	1.4 ± 0.2

Table 3
Vickers hardness of the as-received and of the material ECAPed by 1 pass, 2 passes and 4 passes.

	As-received	ECAP		
		1 pass	2 passes	4 passes
HV	65.1 ± 5.1	69.2 ± 4.1	65.6 ± 5.7	57.9 ± 1.9

brittle fracture mode experienced by 1 pass ECAPed samples to the ductile markedly ductile fracture behavior of 2 and 4 passes ECAPed samples (Fig. 12c and g and Fig. 12d and h, respectively).

3.5.2. Samples tested in SBF

The fracture surfaces of the samples tested in SBF are reported in Fig. 13, and in particular the fractographies of the samples in the as-received condition are reported in Fig. 13a and e, while those of the ECAPed samples are reported in Fig. 13b and f, Fig. 13c and g and Figs. 13d and h for 1, 2 and 4 passes of ECAP, respectively.
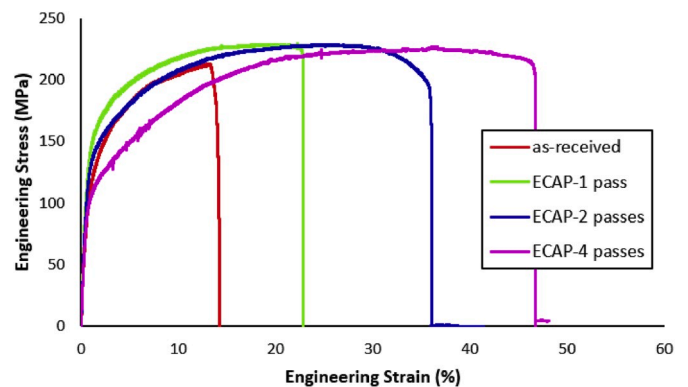

Fig. 7. Engineering stress-strain curves of as-received AZ31 alloy (red) and ECAPed by 1 pass (green), 2 passes (blue) and 4 passes (fuchsia).

Table 4
Mechanical properties from Fig. 7.

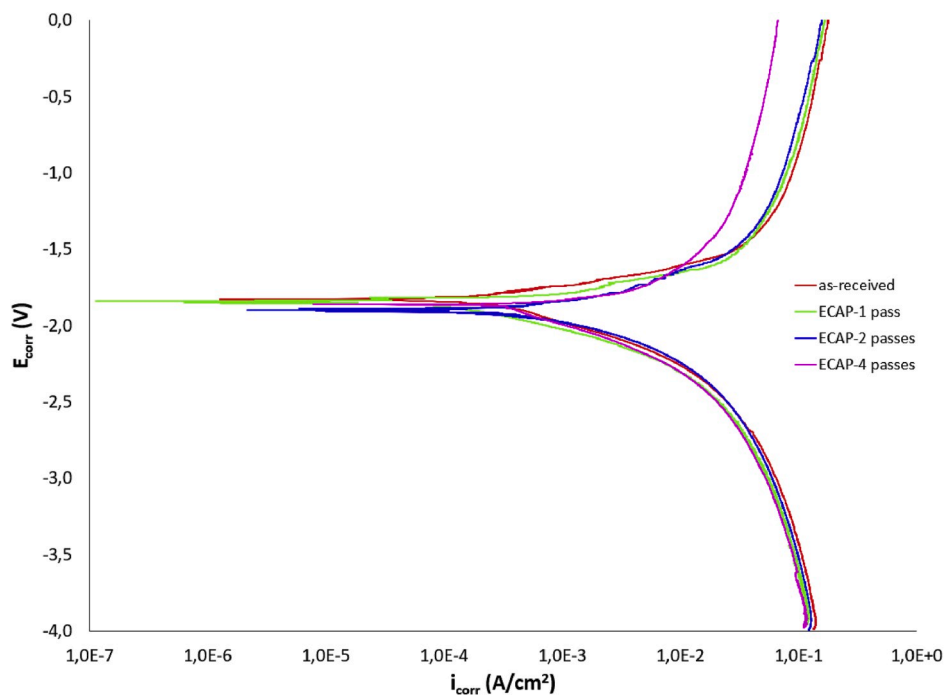|	As-received	ECAP		
		1 pass	2 passes	4 passes
σ_y (MPa)	97.7 ± 4.8	122.7 ± 5.3	109.5 ± 4.1	86.0 ± 3.7
UTS (MPa)	212.9 ± 5.6	229.1 ± 4.3	228.8 ± 2.5	227.2 ± 3.2
ε_f (%)	14.2 ± 1.9	22.8 ± 1.0	36.0 ± 0.7	46.8 ± 1.3

Fig. 8. Potentiodynamic polarization curves for the as-received and ECAPed AZ31 samples in SBF solution at 37 °C.

Table 5
Electrochemical corrosion data extrapolated from Fig. 8.

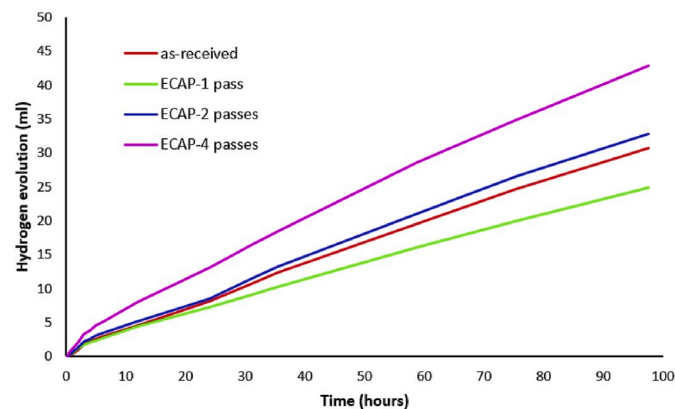|	As-received	ECAP		
		1 pass	2 passes	4 passes
E_{corr} (V)	−1.83 ± 0.018	−1.84 ± 0.015	−1.90 ± 0.025	−1.86 ± 0.013
i_{corr} (μA/cm²)	215.6 ± 4.1	83.5 ± 10.6	286.5 ± 8.7	349.1 ± 13.8

Fig. 9. Hydrogen evolved from the as-received and ECAPed AZ31 alloy.

The surface fracture appearance of the samples tested in SBF are characterized by transgranular and intergranular cracks. The sample in the as-received condition shows a combination of the two crack typologies, while the sample subjected to 1 pass of ECAP shows a predominance of intergranular cracking. However, further increasing the number of ECAP passes are shown to change the failure mode from intergranular fracture of samples subjected to 1 pass of ECAP to a predominance of transgranular fracture of the samples subjected to 4 passes of ECAP.

In addition, the tilted views of the gauge section are reported in Fig. 14. A small number of secondary cracks were shown by the sample in the as-received condition (Fig. 14a). The effect of one pass of ECAP is shown to reduce the number of cracks, that were also less deep than in the as-received material (Fig. 14b). However, denser and deeper secondary cracks were evident in the samples subjected to 2 passes of ECAP (Fig. 14c), and even more visible in the samples subjected to 4 passes of ECAP, where corrosion pits are evident (Fig. 14d).

4. Discussion

Mg and its alloys have been widely studied as materials for temporary applications such as stents and bone fixators. However, their use has been hampered by their high corrosion rate and by their high susceptibility to corrosion-assisted-cracking phenomena such as SCC and CF. The corrosion rate of Mg and its alloys is widely known to be influenced by several parameters, such as surface roughness, grain size, crystallographic orientation of the grains, residual stresses and electrolyte composition (op't Hoog et al., 2008; Bagherifard et al., 2018). In particular, the reduction of grain size has been extensively studied as an approach to reduce the corrosion rate due to the increased stability of the oxide layer associated with fine grains. In this perspective, several processing techniques have been investigated and ECAP has been proved to be an effective way to reduce the grain size. However, the data regarding the effect of ECAP on corrosion of Mg and its alloys are contradicting. In fact, while on the one hand ECAP improves the corrosion resistance due to the reduced grain size, on the other hand it decreases the corrosion resistance orienting the basal planes towards the shearing directions (Pu et al., 2012). Moreover, to the best of the authors' knowledge, the effect of ECAP on the SCC susceptibility has never been investigated before. Therefore, in the present study, 1, 2 and 4 passes of ECAP were applied to an AZ31 alloy with the aim to evaluate their effect on the SCC susceptibility. Furthermore, microstructural analyses, mechanical characterizations, potentiodynamic polarization curves, hydrogen evolution experiments and Scanning Electron Microscopy (SEM) analyses of the fracture surfaces were carried out in order to relate the observed SCC susceptibilities to the corrosion behavior and consequently to the microstructure and crystallographic orientation of the grains.
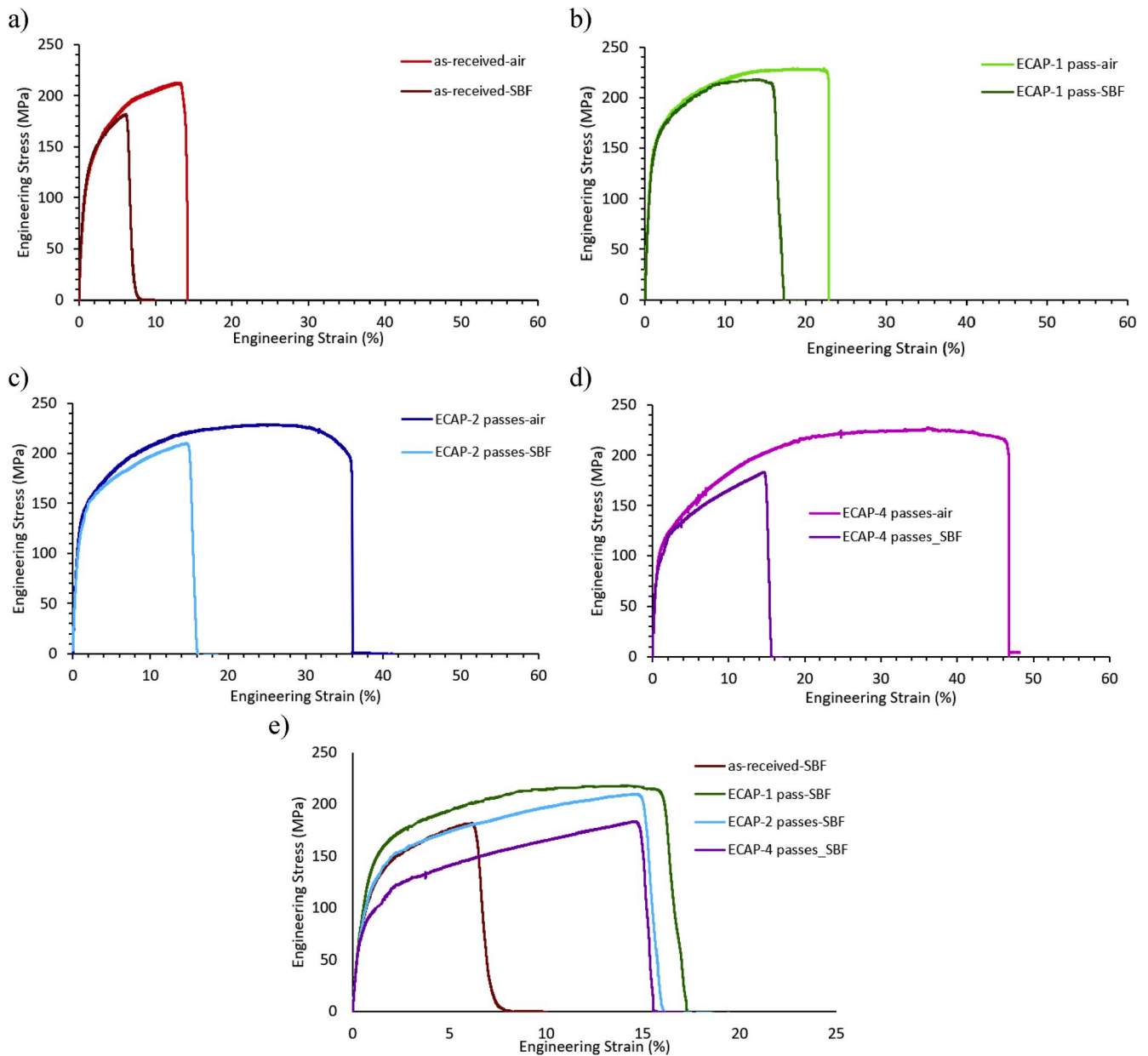
Fig. 10. Engineering stress-strain curves of as-received AZ31 alloy (a) and ECAPed by 1 pass (b), 2 passes (c) and 4 passes (d) tested in SBF. For sake of comparison, the corresponding Engineering stress-strain curves of the samples tested in air are also reported; in Fig. 10e the results of the samples tested in SBF are compared.

Table 6
Mechanical properties of the as-received material and of the material ECAPed tested in SBF.

	As-received	ECAP		
		1 pass	2 passes	4 passes
UTS (MPa)	181.6 ± 8.2	218.0 ± 3.9	210.0 ± 5.4	183.3 ± 6.1
ε_f (%)	6.5 ± 1.6	16.2 ± 1.1	15.1 ± 2.1	14.9 ± 1.7

Dealing with the SCC susceptibility, from the experimental results (Figs. 10 and 11) it can be seen that the application of one pass of ECAP has been proved to yield higher resistance to SCC in SBF compared to the material in the as-received conditions. The susceptibility indices I_{UTS} and I_{ε} of samples subjected to one pass of ECAP were in fact decreased up to approximately 67% and 47%, respectively, indicating a strengthened response to the combined application of mechanical load and corrosive environment. However, further ECAP processing led to an
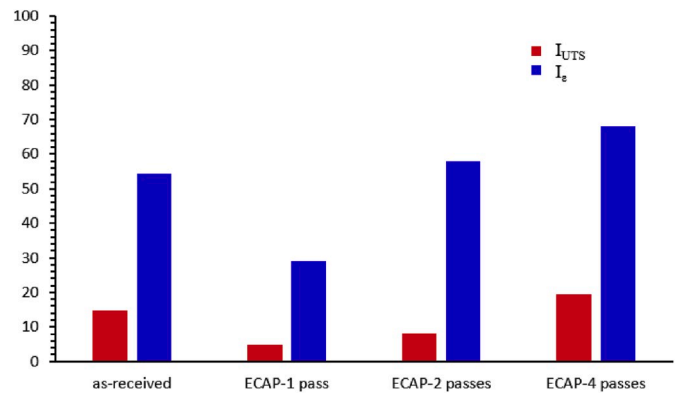
Fig. 11. SCC susceptibility indexes for as-received material and for the ECA-Ped material.
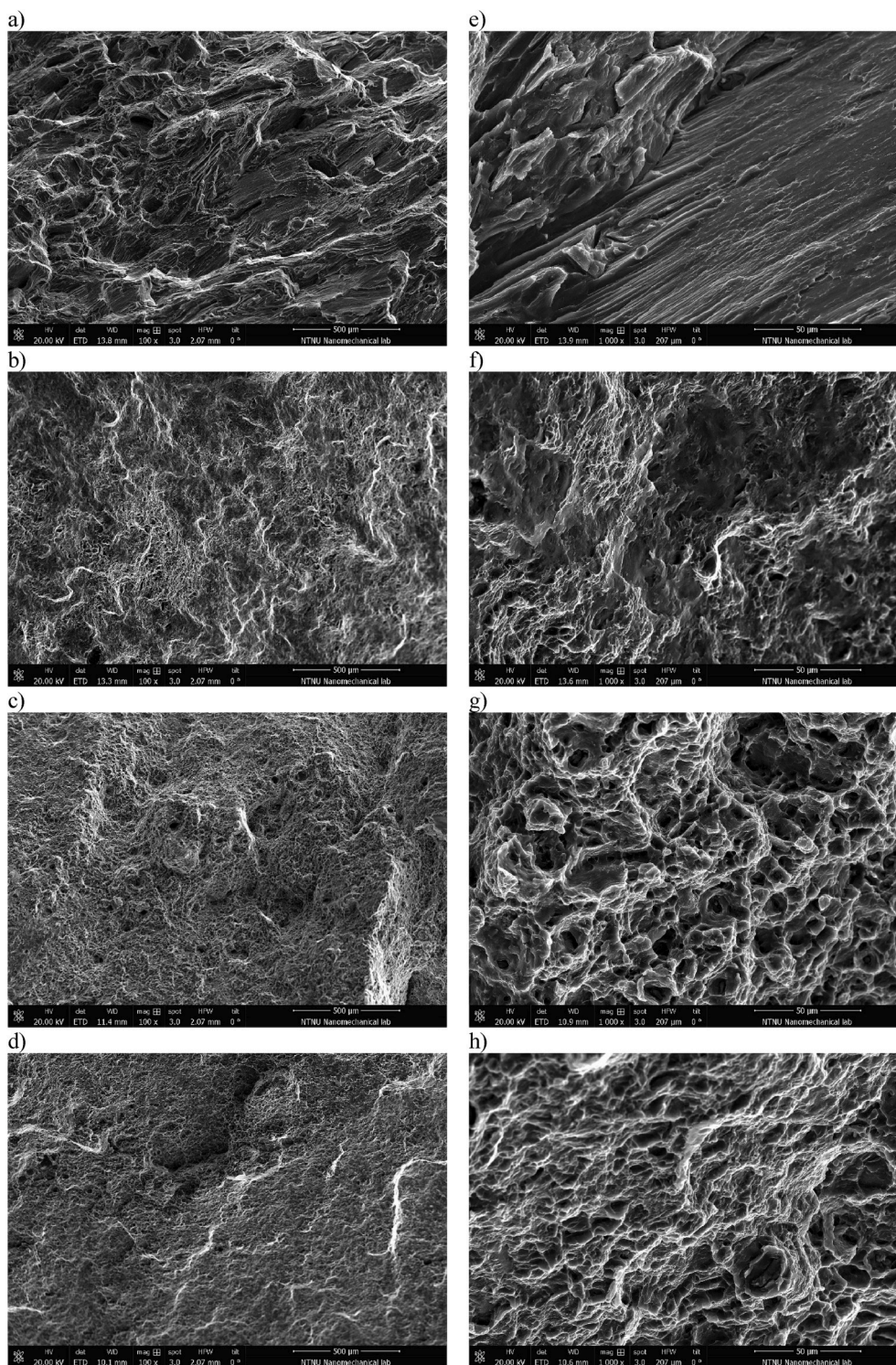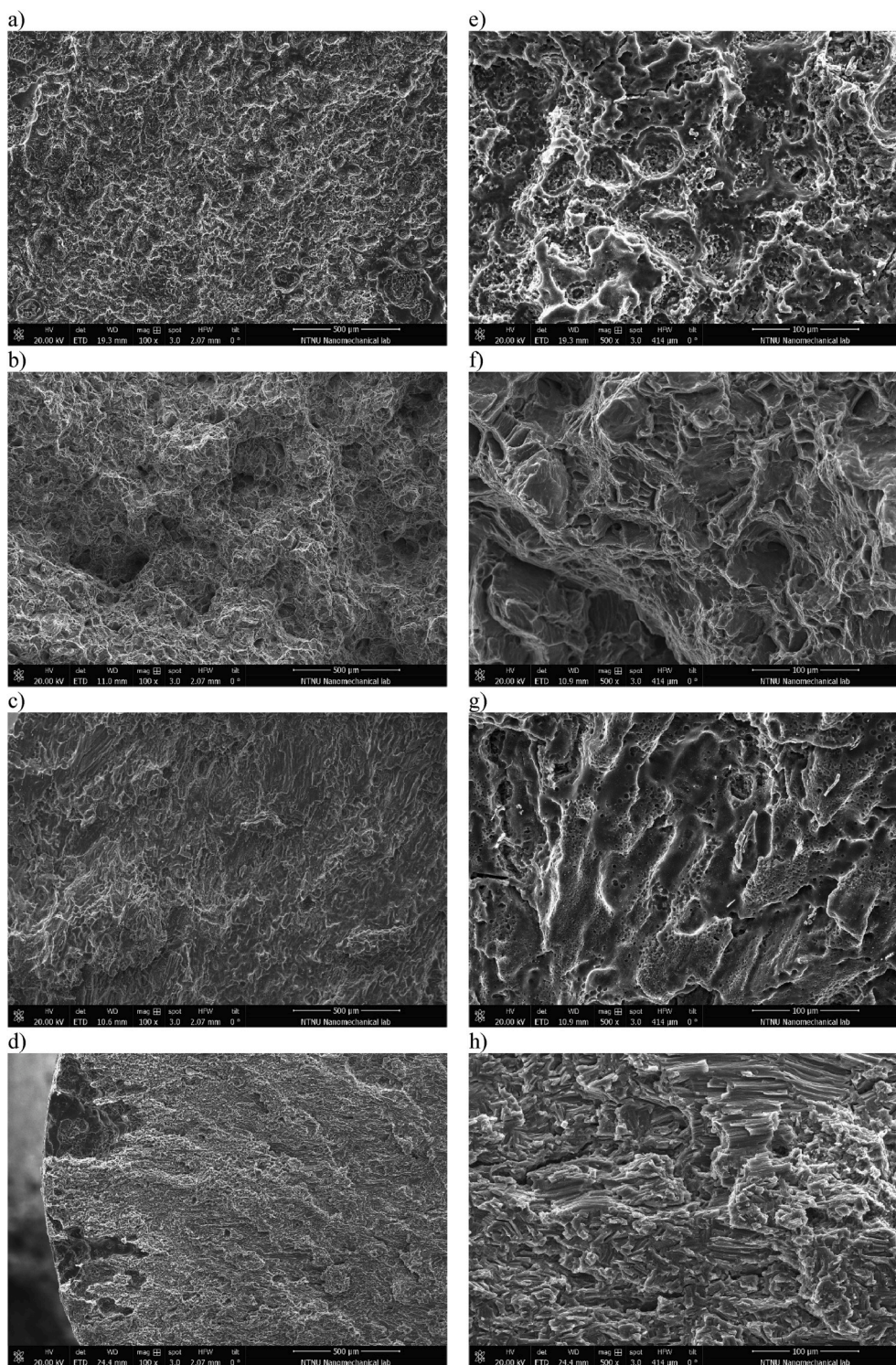
Fig. 12. Fracture surfaces of the as received material (a and e) and of the material ECAPed by 1 pass (b and f), 2 passes (c and g) and 4 passes (d and h) tested in air.

increased susceptibility to SCC, that, in the case of the samples subjected to 4 passes of ECAP, resulted to be even higher than the SCC susceptibility of the as-received material. These results can be linked to the different corrosion behavior of the material subject to different ECAP treatments.

SCC of Mg alloys is widely attributed to the combination of two mechanisms, namely the anodic dissolution and cleavage-like fracture due to hydrogen embrittlement (Winzer et al., 2005). The rupture of the protective $Mg(OH)_2$ film due to the anodic dissolution or due to

mechanical loads allows the hydrogen evolved from the corrosion process to enter into the matrix and to embrittle the material, leading to a premature fracture (Jafari et al., 2015). Pitting is reported as main precursor for the initiation of SCC cracks (Stampella et al., 1984; Raja and Padekar, 2013). The lower the tendency of a material to be subjected to pitting and to localized corrosion, the lower the corrosion rate and hence the SCC susceptibility. The increased resistance to pitting (Fig. 14) and to corrosion (Figs. 8 and 9) of samples subjected to 1 pass of ECAP reduced the SCC susceptibility of this material. The improved

Fig. 13. Fracture surfaces of the as received material (a and e) and of the material ECAPed by 1 pass (b and f), 2 passes (c and g) and 4 passes (d and h) tested in SBF.

corrosion behavior can be linked to the reduced grain size compared to the as-received material (Fig. 5). In fact, after 1 pass of ECAP, the grain size was reduced from 27.5 to 8.3 μm as a consequence of dynamic recrystallization (DRX), where the nucleation of new fine grains occurs along the grain and twin boundaries during strain accumulation (Figueiredo and Langdon, 2010). These results agree with those obtained by Minarik et al. (Minárik et al., 2017) that reported the reduction of almost 15% in the corrosion rate after 12 passes of ECAP to be a consequence of the decrease in the grain size from 21 μm to 1.7 μm. This reduction in

grain size hinders the corrosion due to three mechanisms. Firstly, the grain boundary acts as a physical corrosion barrier; smaller grain sizes yield an increased number of grain boundaries and hence a reduced corrosion rate (Aung and Zhou, 2010). Secondly, the geometrical mismatches between the MgO layer and the metallic substrate arising when the oxide forms causes tensile stresses in the oxide, thereby increasing its propensity for cracking. A fine-grained microstructure is known to relieve these stresses (Birbilis et al., 2010). This leads to a reduced degree of oxide cracking that provides a better surface coverage and hence
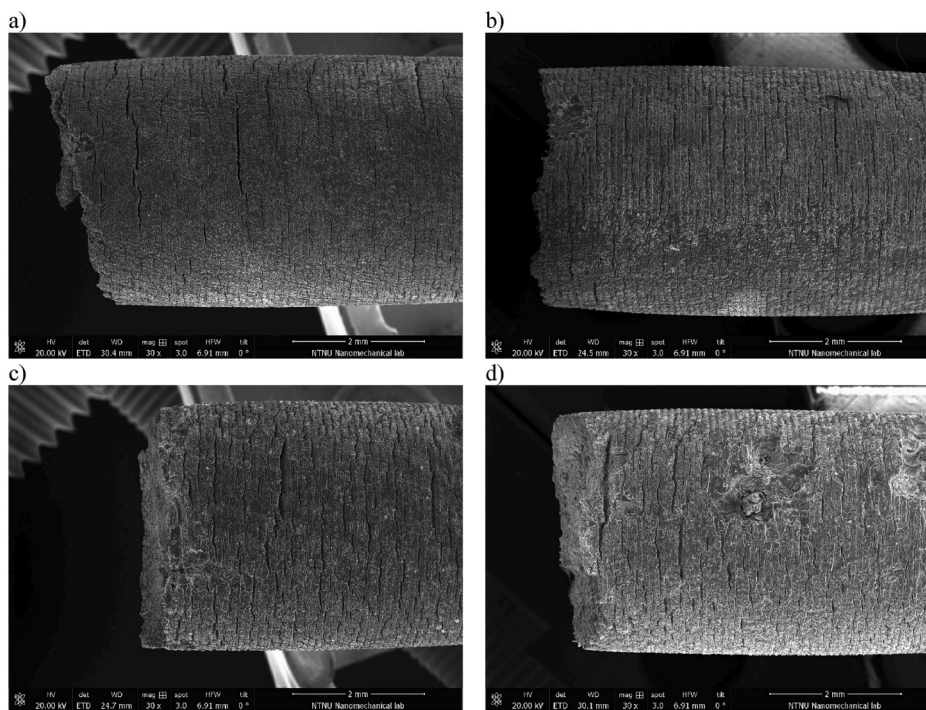
Fig. 14. SEM fractographies of the gauge section of the as received material (a) and of the material ECAPed by 1 pass (b), 2 passes (c) and 4 passes (d) tested in SBF.

an increased corrosion resistance (Orlov et al., 2011). Thirdly, the positive effect of small grain sizes on corrosion resistance can be attributed to the rapid formation of passivation oxide films at grain boundaries, which provides nucleation sites for passivating oxide films and the higher interfacial adherence of the passive film (MgO) at grain boundaries compared with the bulk (Birbilis et al., 2010; Ralston et al., 2010) that provide a barrier to the corrosive fluid.

However, the results concerning the corrosion performances of the samples obtained with 2 and 4 passes of ECAP (Figs. 8 and 9) are in contrast with what just stated. In fact, although the grain size is decreased, the corrosion resistance gets worse and becomes even lower than that of the as-received samples for the samples subjected to 4 passes of ECAP. The deterioration of the corrosion resistance despite the decrease of the grain size has been reported also elsewhere (Shahar et al., 2017; Song et al., 2011; Gu et al., 2011) and can be explained with the texture evolution within the material. ECAP is reported to modify the texture of the material due to the heavy shear strains imposed. The critical resolved shear stress (CRSS) for basal plane slip is 100 times lower than that for non-basal plane slip (Mukai et al., 2001). The basal plane hence rearranges to the shearing direction, which is inclined by 45° with respect to the "extrusion" direction. However, the basal plane is reported to be more corrosion resistance than the non-basal planes due to its high atomic density (Song, 2012). The activation energy required for the dissolution of an atom from a crystal is proportional to the atomic packing density of the crystallographic plane. As more and more basal planes will be rearranged at 45° from the "extrusion" direction with increasing number of ECAP passes, the corrosion resistance is reduced (Figs. 8 and 9) and the susceptibility to pitting is increased (Fig. 14), thus leading to enhanced SCC susceptibility (Fig. 11). In addition, the arrangement of the basal planes along with the shearing direction (oriented at 45° to the stress axis) is of major importance from a mechanical point of view. Basal planes are in fact in positions favourable for basal slip, inducing an increased ductility with an increase of the number of passes (Fig. 7 and Table 3) (Gzyl et al., 2015; Kim and Jeong, 2005). This affect also the strength of the material. Dealing with the yield strength, the reduction in grain size led to an increment by 30%. However further ECAP passes reduced the yield strength although the grain size remained

approximately constant. We hypothesize that this is due to the texture evolution occurring after 2 and 4 ECAP passes, that, rotating the basal planes towards the shearing direction, reduced the strength necessary to activate the basal slip systems. This is in agreement with previous work (Agnew et al., 2004). The texture softening was also hypothesized to be responsible of the results regarding the UTS (Fig. 7 and Table 4). In fact, after 1 pass of ECAP, the UTS is shown to be almost independent on the number of passes, slightly decreasing. A similar behaviour was observed by Gopi et al. (2017). In their work, an AM90 alloy was subjected up to 4 passes of ECAP. Although the grain size constantly decreased, the UTS was found to be maximum after 2 passes, and to decrease with further ECAP processing. They related this decrease in strength to the texture softening, in accordance with Shi et al. (Shi et al., 2019) and Hassani et al. (2011). Similarly, the effect of ECAP on the hardness measurements can also be related to the orientation of basal slip systems. In fact, although the Hall-Petch equation would suggest an increase in hardness as the number of passes increases as a consequence of the reduced grain size, the results reported in Table 3 shows that the hardness increases after 1 pass of ECAP, while it decreases after 2 and 4 passes. These results are in agreement with those reported by Muralidhar et al. (2013), where the hardness of an AZ31 alloy was found to decrease after 2 passes despite the reduction in grain size. This is due to the effect of the texture evolution during the ECAP process that becomes predominant over the grain reduction. Since the basal grains that are characterized by a higher hardness than that their non-basal counterparts (Sahoo et al., 2015), the arrangement of the basal planes towards the shearing direction are thus responsible for the drop in hardness.

5. Conclusion

In this study, the effect of ECAP processing on the stress corrosion cracking (SCC) susceptibility of the AZ31 Mg alloy was assessed. SSRTs at a strain rate of $3.5 \cdot 10^{-6}$ s^{-1} were carried out in SBF at 37 °C. In addition, potentiodynamic polarization tests, hydrogen evolution tests, a mechanical characterization of the treated and un-treated alloy by means of tensile tests and hardness measurements and fracture surfaces analyses were carried out to explain the different observed SCC

susceptibilities in terms of microstructure and crystallographic orientation of the grains.

The main findings can be summarized as follows:

- Samples subjected to 1 pass of ECAP are characterized by the lowest susceptibility in SBF at body temperature (I_{UTS} and the I_ε were found to be 4.8% and 28.9%, respectively). Further ECAP processing (2 and 4 passes) are reported to deteriorate the SCC susceptibility (I_{UTS} and the I_ε were found to be 8.2% and 58.1% and 19.3% and 68.2% for 2 and 4 passes, respectively). Their SCC susceptibility becomes higher than that of the material in the as-received condition (I_{UTS} and the I_ε were found to be 14.7% and 54.2%, respectively).

- The improved corrosion resistance after one pass of ECAP (i_{corr} is almost three times lower than that obtained for the as-received material and the evolved hydrogen is reduced of almost 20%) was held responsible of the enhancement in the SCC susceptibility. This was related to the reduced grain size that allows both a faster formation of the passivating surface oxide and a better surface coverage provided by this oxide layer as a consequence of a reduced degree of oxide cracking.

- The crystallographic orientation was hypothesized the cause of the deterioration in the SCC after 2 and 4 passes of ECAP. The alignments of basal planes with the shearing direction as a consequence of ECAP can in fact explain the detrimental effects on the corrosion resistance shown by the potentiodynamic polarization curves (i_{corr} increases from 83.5 $\mu A/cm^2$ for 1 pass of ECAP to 286.5 and to 349.1 $\mu A/cm^2$ for 2 and 4 passes of ECAP, respectively) and by the hydrogen evolution tests (the hydrogen evolved from the as-received material increases by 7% and 39% for 2 and 4 passes of ECAP, respectively). Further evidences of the alignments of basal planes with the shearing direction are the results of the mechanical tests and of the hardness measurements.

It can be concluded that the ECAP process is an effective method to decrease the AZ31 sensitivity to SCC due to the great grain refinement that can be obtained. However, when the texture evolution becomes predominant over the grain refinement effect, ECAP processing results become detrimental to SCC susceptibility.

Author statement

References

N.d.). ASTM G5 - 14 Standard Reference Test Method for Making Potentiodynamic Anodic Polarization Measurements.

Agnew, S.R., Horton, J.A., Lillo, T.M., Brown, D.W., 2004. Enhanced ductility in strongly textured magnesium produced by equal channel angular processing. Scripta Mater. 50 (3), 377–381. https://doi.org/10.1016/j.scriptamat.2003.10.006.

Akahori, T., Niinomi, M., Fukunaga, K.-I., Inagaki, I., 2000. Effects of microstructure on the short fatigue crack initiation and propagation characteristics of biomedical α/β titanium alloys. Metall. Mater. Trans. A 31 (8), 1949–1958. https://doi.org/10.1007/s11661-000-0222-z.

Albrektsson, T., Brånemark, P.-I., Hansson, H.-A., Lindström, J., 1981. Osseointegrated titanium implants: Requirements for Ensuring a long-lasting, direct bone-to-implant Anchorage in man. Acta Orthop. Scand. 52 (2), 155–170. https://doi.org/10.3109/17453678108991776.

Antunes, R.A., de Oliveira, M.C.L., 2012. Corrosion fatigue of biomedical metallic alloys: mechanisms and mitigation. Acta Biomater. 8 (3), 937–962. https://doi.org/10.1016/j.actbio.2011.09.012.

ASTM E92, 2017. ASTM E92-17, Standard Test Methods for Vickers Hardness and Knoop Hardness of Metallic Materials. ASTM Int., pp. 1–27. https://doi.org/10.1520/E0092-17

Aung, N.N., Zhou, W., 2010. Effect of grain size and twins on corrosion behaviour of AZ31B magnesium alloy. Corrosion Sci. 52 (2), 589–594. https://doi.org/10.1016/J.CORSCI.2009.10.018.

Bagherifard, S., Hickey, D.J., Fintová, S., Pastorek, F., Fernandez-Pariente, I., Bandini, M., Webster, T.J., Guagliano, M., 2018. Effects of nanofeatures induced by severe shot peening (SSP) on mechanical, corrosion and cytocompatibility properties of magnesium alloy AZ31. Acta Biomater. 66, 93–108. https://doi.org/10.1016/J.ACTBIO.2017.11.032.

Bauer, T.W., Schils, J., 1999. The pathology of total joint arthroplasty.II. Mechanisms of implant failure. Skeletal Radiol. 28 (9), 483–497.

Beech, I.B., Sunner, J.A., Arciola, C.R., Cristiani, P., 2006. Microbially-influenced corrosion: damage to prostheses, delight for bacteria. Int. J. Artif. Organs 29 (4), 443–452.

Bertolini, R., Bruschi, S., Ghiotti, A., Pezzato, L., Dabalà, M. (2017). [35].

Birbilis, N., Ralston, K.D., Virtanen, S., Fraser, H.L., Davies, C.H.J., 2010. Grain character influences on corrosion of ECAPed pure magnesium. Corrosion Eng. Sci. Technol. 45 (3), 224–230. https://doi.org/10.1179/147842209X12559428167805.

Bobby Kannan, M., Dietzel, W., Blawert, C., Atrens, A., Lyon, P., 2008. Stress corrosion cracking of rare-earth containing magnesium alloys ZE41, QE22 and Elektron 21 (EV31A) compared with AZ80. Mater. Sci. Eng. A 480 (1–2), 529–539. https://doi.org/10.1016/J.MSEA.2007.07.070.

Bryła, K., Dutkiewicz, J., Lityńska-dobrzyńska, L., Rokhlin, L.L., Kurtyka, P., 2012. Influence of number of ecap passes on microstructure and mechanical properties of az31 magnesium alloy. Arch. Metall. Mater. 57 (3), 711–717. https://doi.org/10.2478/v10172-012-0077-5.

Chen, Q., Thouas, G.A., 2015. Metallic implant biomaterials. Mater. Sci. Eng. R Rep. 87, 1–57. https://doi.org/10.1016/J.MSER.2014.10.001.

Chen, L., Sheng, Y., Zhou, H., Li, Z., Wang, X., Li, W., 2018. Influence of a MAO + PLGA coating on biocorrosion and stress corrosion cracking behavior of a magnesium alloy in a physiological environment. Corrosion Sci. https://doi.org/10.1016/J.CORSCI.2018.12.005.

Choudhary, L., Raman, R.K.S., 2011. Acta Biomaterialia Magnesium alloys as body implants : fracture mechanism under dynamic and static loadings in a physiological environment. Acta Biomater. 8 (2), 916–923. https://doi.org/10.1016/j.actbio.2011.10.031.

Choudhary, L., Singh Raman, R.K., Hofstetter, J., Uggowitzer, P.J., 2014. In-vitro characterization of stress corrosion cracking of aluminium-free magnesium alloys for temporary bio-implant applications. Mater. Sci. Eng. C 42, 629–636. https://doi.org/10.1016/J.MSEC.2014.06.018.

Dujovne, A.R., Bobyn, J.D., Krygier, J.J., Miller, J.E., Brooks, C.E., 1993. Mechanical compatibility of noncemented hip prostheses with the human femur. J. Arthroplasty 8 (1), 7–22. https://doi.org/10.1016/S0883-5403(06)80102-6.

Engh, C.A., Bobyn, J.D., 1988. The influence of stem size and extent of porous coating on femoral bone resorption after primary cementless hip arthroplasty. Clin. Orthop. Relat. Res. (231), 7–28.

Figueiredo, R.B., Langdon, T.G., 2010. Grain refinement and mechanical behavior of a magnesium alloy processed by ECAP. J. Mater. Sci. 45, 4827–4836.

Gao, Y., Yerokhin, A., Matthews, A., 2015. Mechanical behaviour of cp-magnesium with duplex hydroxyapatite and PEO coatings. Mater. Sci. Eng. C 49, 190–200. https://doi.org/10.1016/J.MSEC.2014.12.081.

Ge, Q., Dellasega, D., Demir, A.G., Vedani, M., 2013. The processing of ultrafine-grained Mg tubes for biodegradable stents. Acta Biomater. 9 (10), 8604–8610. https://doi.org/10.1016/j.actbio.2013.01.010.

Ginebra, M.P., Traykova, T., Planell, J.A., 2006. Calcium phosphate cements as bone drug delivery systems: a review. J. Contr. Release 113 (2), 102–110. https://doi.org/10.1016/j.jconrel.2006.04.007.

Gopi, K.R., Shivananda Nayaka, H., Sahu, S., 2017. Microstructural evolution and strengthening of AM90 magnesium alloy processed by ECAP. Arabian J. Sci. Eng. 42 (11), 4635–4647. https://doi.org/10.1007/s13369-017-2574-3.

Gu, X.N., Li, N., Zheng, Y.F., Kang, F., Wang, J.T., Ruan, L., 2011. In vitro study on equal channel angular pressing AZ31 magnesium alloy with and without back pressure. Mater. Sci. Eng. B 176 (20), 1802–1806. https://doi.org/10.1016/J.MSEB.2011.04.003.

Gzyl, M., Rosochowski, A., Pesci, R., Olejnik, L., Yakushina, E., Wood, P., 2014. Mechanical properties and microstructure of az31b magnesium alloy processed by I-ECAP. Metall. Mater. Trans. A Phys. Metall. Mater. Sci. 45 (3), 1609–1620. https://doi.org/10.1007/s11661-013-2094-z.

Gzyl, M., Rosochowski, A., Boczkal, S., Olejnik, L., 2015. The role of microstructure and texture in controlling mechanical properties of AZ31B magnesium alloy processed by I-ECAP. Mater. Sci. Eng. A 638, 20–29. https://doi.org/10.1016/j.msea.2015.04.055.

Hanawa, T., 2010. Overview of Metals and Applications. Metals for Biomedical Devices. Elsevier, pp. 3–24.

Hänzi, A.C., Sologubenko, A.S., Uggowitzer, P.J., 2009. Design strategy for new biodegradable Mg–Y–Zn alloys for medical applications. Int. J. Mater. Res. 100 (8), 1127–1136. https://doi.org/10.3139/146.110157.

Hassani, F.Z., Ketabchi, M., Hassani, M.T., 2011. Effect of twins and non-basal planes activated by equal channel angular rolling process on properties of AZ31 magnesium alloy. J. Mater. Sci. 46 (24), 7689–7695. https://doi.org/10.1007/s10853-011-5748-5.

Jacobs, J.J., Gilbert, J.L., Urban, R.M., 1998. Corrosion of metal orthopaedic implants. J. Bone Joint Surg. Am. 80 (2), 268–282.

Jacobs, J.J., Hallab, N.J., Skipor, A.K., Urban, R.M., 2003. Metal degradation products: a cause for concern in metal-metal bearings? Clin. Orthop. Relat. Res. (417), 139–147. https://doi.org/10.1097/01.blo.0000096810.78689.62.

Jafari, S., Harandi, S.E., Singh Raman, R.K., 2015. A review of stress-corrosion cracking and corrosion fatigue of magnesium alloys for biodegradable implant applications. JOM (J. Occup. Med.) 67 (5), 1143–1153. https://doi.org/10.1007/s11837-015-1366-z.

Jafari, S., Raman, R.K.S., Davies, C.H.J., Hofstetter, J., Uggowitzer, P.J., Löffler, J.F., 2017. Stress corrosion cracking and corrosion fatigue characterisation of MgZn1Ca0.3 (ZX10) in a simulated physiological environment. J. Mech. Behav. Biomed. Mater. 65, 634–643. https://doi.org/10.1016/J.JMBBM.2016.09.033.

Jafari, S., Raman, R.K.S., Davies, C.H.J., 2018. Stress corrosion cracking of an extruded magnesium alloy (ZK21) in a simulated body fluid. Eng. Fract. Mech. 201, 47–55. https://doi.org/10.1016/J.ENGFRACMECH.2018.09.002.

Kannan, M.B., Raman, R.K.S., 2008. In vitro degradation and mechanical integrity of calcium-containing magnesium alloys in modified-simulated body fluid. Biomaterials 29 (15), 2306–2314. https://doi.org/10.1016/J.BIOMATERIALS.2008.02.003.

Kerner, J., Huiskes, R., van Lenthe, G.H., Weinans, H., van Rietbergen, B., Engh, C.A., Amis, A.A., 1999. Correlation between pre-operative periprosthetic bone density and post-operative bone loss in THA can be explained by strain-adaptive remodelling. J. Biomech. 32 (7), 695–703. https://doi.org/10.1016/S0021-9290(99)00041-X.

Kim, W.J., Jeong, H.T., 2005. Grain-size strengthening in equal-channel-angular-pressing processed AZ31 Mg alloys with a constant texture. Mater. Trans. 46 (2), 251–258. https://doi.org/10.2320/matertrans.46.251.

Kokubo, T., Takadama, H., 2006. How useful is SBF in predicting in vivo bone bioactivity? Biomaterials 27 (15), 2907–2915. https://doi.org/10.1016/J.BIOMATERIALS.2006.01.017.

Kutniy, K.V., Papirov, I.I., Tikhonovsky, M.A., Pikalov, A.I., Sivtzov, S.V., Pirozhenko, L.A., Shokurov, V.S., Shkuropatenko, V.A., 2009. Influence of grain size on mechanical and corrosion properties of magnesium alloy for medical implants. Mater. Werkst. 40 (4), 242–246. https://doi.org/10.1002/mawe.200900434.

Linderov, M., Vasilev, E., Merson, D., Markushev, M., Vinogradov, A., 2017. Corrosion fatigue of fine grain Mg-Zn-Zr and Mg-Y-Zn alloys. Metals (Basel). 8 (1), 20. https://doi.org/10.3390/met8010020.

Minárik, P., Jablonská, E., Král, R., Lipov, J., Ruml, T., Blawert, C., Hadzima, B., Chmelík, F., 2017. Effect of equal channel angular pressing on in vitro degradation of LAE442 magnesium alloy. Mater. Sci. Eng. C 73, 736–742. https://doi.org/10.1016/J.MSEC.2016.12.120.

Mohajernia, S., Pour-Ali, S., Hejazi, S., Saremi, M., Kiani-Rashid, A.-R., 2018. Hydroxyapatite coating containing multi-walled carbon nanotubes on AZ31 magnesium: mechanical-electrochemical degradation in a physiological environment. Ceram. Int. 44 (7), 8297–8305. https://doi.org/10.1016/J.CERAMINT.2018.02.015.

Mukai, T., Yamanoi, M., Watanabe, H., Higashi, K., 2001. Ductility enhancement in AZ31 magnesium alloy by controlling its grain structure. Scripta Mater. 45 (1), 89–94. https://doi.org/10.1016/S1359-6462(01)00996-4.

Muralidhar, A., Narendranath, S., Shivananda Nayaka, H., 2013. Effect of equal channel angular pressing on AZ31 wrought magnesium alloys. J. Magnes. Alloy. 1 (4), 336–340. https://doi.org/10.1016/j.jma.2013.11.007.

N.d.). http://share.iofbonehealth.org/EU-6-Material/Reports/IOF%20Report_EU.pdf. Available at: http://share.iofbonehealth.org/EU-6-Material/Reports/IOF Report_EU.pdf. [accessed November 20, 2019].

opt'Hoog, C., Birbilis, N., Estrin, Y., 2008. Corrosion of pure Mg as a function of grain size and processing route. Adv. Eng. Mater. 10 (6), 579–582. https://doi.org/10.1002/adem.200800046.

Orlov, D., Ralston, K.D., Birbilis, N., Estrin, Y., 2011. Enhanced corrosion resistance of Mg alloy ZK60 after processing by integrated extrusion and equal channel angular pressing. Acta Mater. 59 (15), 6176–6186. https://doi.org/10.1016/j.actamat.2011.06.033.

Peron, M., Torgersen, J., Berto, F., 2017. Mg and its alloys for biomedical applications: exploring corrosion and its interplay with mechanical failure. Metals (Basel) 7 (7), 252. https://doi.org/10.3390/met7070252.

Peron, M., Bertolini, R., Ghiotti, A., Torgersen, J., Bruschi, S., Berto, F., 2020. Enhancement of stress corrosion cracking of AZ31 magnesium alloy in simulated body fluid thanks to cryogenic machining. J. Mech. Behav. Biomed. Mater. 101, 103429. https://doi.org/10.1016/J.JMBBM.2019.103429.

Pound, B.G., 2014a. Corrosion behavior of metallic materials in biomedical applications . I . Ti and its alloys, 32, 1–20. https://doi.org/10.1515/corrrev-2014-0007.

Pound, B.G., 2014b. Corrosion behavior of metallic materials in biomedical applications . II . Stainless steels and Co-Cr alloys, 32, 21–41. https://doi.org/10.1515/corrrev-2014-0008.

Pu, Z., Song, G.-L., Yang, S., Outeiro, J.C., Dillon, O.W., Puleo, D.A., Jawahir, I.S., 2012. Grain refined and basal textured surface produced by burnishing for improved corrosion performance of AZ31B Mg alloy. Corrosion Sci. 57, 192–201. https://doi.org/10.1016/J.CORSCI.2011.12.018.

Raja, V.S., Padekar, B.S., 2013. Role of chlorides on pitting and hydrogen embrittlement of Mg–Mn wrought alloy. Corrosion Sci. 75, 176–183. https://doi.org/10.1016/J.CORSCI.2013.05.030.

Ralston, K.D., Birbilis, N., Davies, C.H.J., 2010. Revealing the relationship between grain size and corrosion rate of metals. Scripta Mater. 63 (12), 1201–1204. https://doi.org/10.1016/J.SCRIPTAMAT.2010.08.035.

Rim, K.T., Koo, K.H., Park, J.S., 2013. Toxicological evaluations of rare earths and their health impacts to workers: a literature review. Saf. Health Work 4 (1), 12–26. https://doi.org/10.5491/SHAW.2013.4.1.12.

Rossi, F., Lang, N.P., De Santis, E., Morelli, F., Favero, G., Botticelli, D., 2014. Bone-healing pattern at the surface of titanium implants: an experimental study in the dog,. Clin. Oral Implants Res. 25 (1), 124–131. https://doi.org/10.1111/clr.12097.

Sahoo, S.K., Sabat, R.K., Panda, S., Mishra, S.C., Suwas, S., 2015. Mechanical property of pure magnesium: from orientation perspective pertaining to deviation from basal orientation. J. Mater. Eng. Perform. 24 (6), 2346–2353. https://doi.org/10.1007/s11665-015-1522-1.

Segal, V.M., 1999. Equal channel angular extrusion: from macromechanics to structure formation. Mater. Sci. Eng. A 271 (1–2), 322–333. https://doi.org/10.1016/s0921-5093(99)00248-8.

Shahar, I.A., Hosaka, T., Yoshihara, S., MacDonald, B.J., 2017. Mechanical and corrosion properties of AZ31 Mg alloy processed by equal-Channel Angular pressing and aging. Procedia Eng. 184, 423–431. https://doi.org/10.1016/J.PROENG.2017.04.113.

Shi, Li, Hu, Tan, Zhang, Tian, 2019. Effect of ECAP on the microstructure and mechanical properties of a rolled Mg-2Y-0.6Nd-0.6Zr magnesium alloy. Crystals 9 (11), 586. https://doi.org/10.3390/cryst9110586.

Singh Raman, R.K., Jafari, S., Harandi, S.E., 2015. Corrosion fatigue fracture of magnesium alloys in bioimplant applications: a review. Eng. Fract. Mech. 137, 97–108. https://doi.org/10.1016/j.engfracmech.2014.08.009.

Song, G., 2007. Control of bioSdegradation of biocompatible magnesium alloys. Corrosion Sci. 49 (4), 1696–1701. https://doi.org/10.1016/J.CORSCI.2007.01.001.

Song, G.L., 2012. The effect of texture on the corrosion behavior of AZ31 Mg alloy. JOM 64 (6), 671–679. https://doi.org/10.1007/s11837-012-0341-1.

Song, D., Ma, A.B., Jiang, J.H., Lin, P.H., Yang, D.H., Fan, J.F., 2011. Corrosion behaviour of bulk ultra-fine grained AZ91D magnesium alloy fabricated by equal-channel angular pressing. Corrosion Sci. 53 (1), 362–373. https://doi.org/10.1016/j.corsci.2010.09.044.

Song, G., Atrens, A., StJohn, D., 2013. An Hydrogen Evolution Method for the Estimation of the Corrosion Rate of Magnesium Alloys. Magnesium Technology. John Wiley & Sons, Inc., Hoboken, NJ, USA, pp. 254–262, 2001.

Song, D., Li, C., Liang, N., Yang, F., Jiang, J., Sun, J., Wu, G., Ma, A., Ma, X., 2019. Simultaneously improving corrosion resistance and mechanical properties of a magnesium alloy via equal-channel angular pressing and post pure water annealing. Mater. Des. 166 https://doi.org/10.1016/j.matdes.2019.107621.

Staiger, M.P., Pietak, A.M., Huadmai, J., Dias, G., 2006. Magnesium and its alloys as orthopedic biomaterials: a review. Biomaterials 27, 1728–1734. https://doi.org/10.1016/j.biomaterials.2005.10.003.

Stampella, R.S., Procter, R.P.M., Ashworth, V., 1984. Environmentally-induced cracking of magnesium. Corrosion Sci. 24 (4), 325–341. https://doi.org/10.1016/0010-938X(84)90017-9.

Sumner, D.R., Galante, J.O., 1992. Determinants of stress shielding: design versus materials versus interface. Clin. Orthop. Relat. Res. (274), 202–212.

Teoh, S., 2000. Fatigue of biomaterials: a review. Int. J. Fatig. 22 (10), 825–837. https://doi.org/10.1016/S0142-1123(00)00052-9.

Thirumalaikumarasamy, D., Shanmugam, K., Balasubramanian, V., 2014. Comparison of the corrosion behaviour of AZ31B magnesium alloy under immersion test and potentiodynamic polarization test in NaCl solution. J. Magnes. Alloy. 2 (1), 36–49. https://doi.org/10.1016/J.JMA.2014.01.004.

Turner, T.M., Sumner, D.R., Urban, R.M., Igloria, R., Galante, J.O., 1997. Maintenance of proximal cortical bone with use of a less stiff femoral component in hemiarthroplasty of the hip without cement. An investigation in a canine model at six months and two years. J. Bone Joint Surg. Am. 79 (9), 1381–1390.

Van Rietbergen, B., Huiskes, R., Weinans, H., Sumner, D.R., Turner, T.M., Galante, J.O., 1993. The mechanism of bone remodeling and resorption around press-fitted THA stems. J. Biomech. 26 (4–5), 369–382. https://doi.org/10.1016/0021-9290(93)90001-U.

Wang, H., Estrin, Y., Zúberová, Z., 2008. Bio-corrosion of a magnesium alloy with different processing histories. Mater. Lett. 62 (16), 2476–2479. https://doi.org/10.1016/J.MATLET.2007.12.052.

Winzer, N., Atrens, A., Song, G., Ghali, E., Dietzel, W., Kainer, K.U., Hort, N., Blawert, C., 2005. A critical review of the Stress Corrosion Cracking (SCC) of magnesium alloys. Adv. Eng. Mater. 7 (8), 659–693. https://doi.org/10.1002/adem.200500071.

Witecka, A., Bogucka, A., Yamamoto, A., Máthis, K., Krajňák, T., Jaroszewicz, J., Święszkowski, W., 2016. In vitro degradation of ZM21 magnesium alloy in simulated body fluids. Mater. Sci. Eng. C 65, 59–69. https://doi.org/10.1016/j.msec.2016.04.019.

Wolff, J., 1986. The Law of Bone Remodelling. Springer Berlin Heidelberg, Berlin, Heidelberg.

Xia, K., Wang, J.T., Wu, X., Chen, G., Gurvan, M., 2005. Equal channel angular pressing of magnesium alloy AZ31. Mater. Sci. Eng. A 410 (411), 324–327. https://doi.org/10.1016/j.msea.2005.08.123.